Phase Equilibria, Microstructure, and High-Temperature Strength of TiC-Added Mo-Si-B Alloys

SHIMPEI MIYAMOTO, KYOSUKE YOSHIMI, SEONG-HO HA, TAKAHIRO KANEKO, JUNYA NAKAMURA, TETSUYA SATO, KOUICHI MARUYAMA, RONG TU, and TAKASHI GOTO

TiC was added to Mo-Si-B alloys using a conventional Ar arc-melting technique, and the phase equilibria, microstructure evolution, and high-temperature strength at 1673 K (1400 °C) were investigated. The primary phase changed to Mo solid solution (Mo_{ss}), Mo_5SiB_2 (T_2), or TiC depending on the composition. Following the primary phase solidification, a Mo_{ss} + TiC, Mo_{ss} + T_2, or Mo_{ss} + T_2 + TiC + Mo_2C eutectic reaction took place as the secondary solidification step. In some alloys, Mo_{ss} + T_2 + TiC and Mo_{ss} + T_2 + Mo_2C eutectic reactions were present as higher-order solidification steps. After annealing at 2073 K (1800 °C) for 24 hours, Mo_{ss}, T_2, TiC, and Mo_2C coexisted stably with microstructural coarsening. The coarsening rate was much faster in an alloy with no TiC dispersion, suggesting that TiC has a strong pinning effect on the grain boundary and interface migration. Compression tests conducted at 1673 K (1400 °C) revealed strength properties of almost all the alloys that were better than those of the Mo-Hf-C alloy (MHC). Alloy densities were 9 g/cm^3 or less, which is lighter than pure Mo and MHC (≥10 g/cm^3) and competitive with Ni-base superalloys. TiC-added Mo-Si-B alloys are promising candidates for ultrahigh-temperature materials beyond Ni-base superalloys.

DOI: 10.1007/s11661-013-1779-7
© The Minerals, Metals & Materials Society and ASM International 2013

I. INTRODUCTION

DEMANDS for energy efficiency improvements in heat engines such as gas turbines and jet engines have prompted calls for ultrahigh-temperature materials available above the operating temperature of Ni-base superalloys. The leading candidates for this purpose are Mo-Si-B alloys consisting of Mo solid solution (Mo_{ss}) and Mo_5SiB_2 (T_2) because of their high melting point, excellent high-temperature (creep) strength, and moderate oxidation resistance in the ultrahigh-temperature range.[1–14] However, the low fracture toughness is a drawback, but this can be improved by optimal control of the microstructure and Mo_{ss} volume fraction.[15] The high density is also problematic for structural applications: For example, in turbine rotors, an increase in the weight results in an increase in the centrifugal force, which shortens the creep lifetime of the material. The density of Ni-base superalloys ranges from 8.6 to 9.2 g/cm^3[16] and the density of T_2 is of a similar value: approximately 8.9 g/cm^3.[2,8] However, in the case that T_2 is incorporated with Mo_{ss} (a density of approximately 10.2 g/cm^3[17]), it is unavoidable that the density of a Mo-Si-B alloy becomes higher than that of Ni-base superalloys. Furthermore, the introduction of a large amount of Mo_{ss} into T_2 results in a lowering of the creep strength in the ultrahigh-temperature region.[11,12]

It is well known that Mo and TiC have a eutectic reaction.[18] The eutectic point is at about Mo-23TiC (at. pct) at 2448 K (2175 °C), and the two solid phases stably coexist below the eutectic temperature without any phase transformation. As shown in Figure 1, each phase is soluble in another one at a certain amount, resulting in solid-solution hardening in both phases.[19] This leads to the expectation that TiC may equilibrate with not only Mo but also other phases in the Mo-Si-B system such as Mo_3Si and T_2. Since the melting point and density of TiC are approximately 3433 K (3160 °C)[19] and 4.93 g/cm^3,[20] respectively, TiC may be beneficial for improving the microstructural stability and reducing the weight of Mo-Si-B alloys if it can coexist with the constituent phases. However, to date, there have been no studies on the phase equilibrium or stability of Mo-Si-B alloys with TiC.

The purpose of this study, therefore, is to investigate the phase equilibria of TiC-added Mo-Si-B alloys.

SHIMPEI MIYAMOTO, Graduate Student, formerly with Graduate School of Environmental Studies, Tohoku University, 6-6-02 Aramaki Aza Aoba, Aobaku, Sendai, Miyagi 980-8579, Japan, is now with IHI Corporation, 5292 Aioi, Aioi, Hyogo 678-0041, Japan. KYOSUKE YOSHIMI and KOUICHI MARUYAMA, Professors, are with Graduate School of Engineering, Tohoku University. Contact e-mail: yoshimi@material.tohoku.ac.jp SEONG-HO HA, Post Doctoral Fellow, formerly with Graduate School of Engineering, Tohoku University, is now with Korea Institute of Industrial Technology, 7-47 Songdo-dong, Yeonsu-ku, Inchon, Korea. TAKAHIRO KANEKO, Graduate Student, JUNYA NAKAMURA, Assistant Professor, are with Graduate School of Environmental Studies, Tohoku University. TETSUYA SATO, Graduate Student, formerly with Graduate School of Environmental Studies, Tohoku University, is now with Central Japan Railway Company, 2-1-85 Konan, Minato-ku, Tokyo, 108-8204, Japan. RONG TU, formerly Associate Professor with Institute for Materials Research, Tohoku University, 2-1-1 Katahira, Aoba-ku, Sendai, Miyagi, Japan, is now Professor with Wuhan University of Technology, 122 Luoshi Road, Wuhan, Hubei 430070, P.R. China. TAKASHI GOTO, Professor, is with Institute for Materials Research, Tohoku University.

Manuscript submitted December 21, 2012.
Article published online May 15, 2013

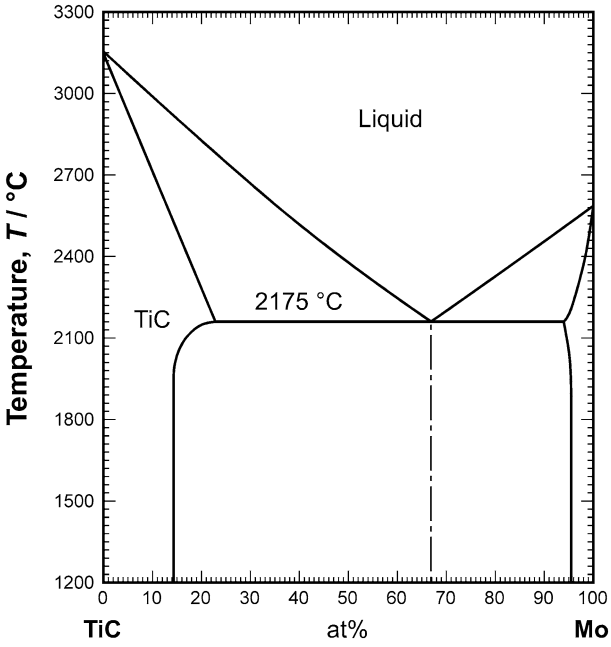

Fig. 1—TiC-Mo pseudo-binary phase diagram.[18]

Solidification pathways and phase equilibria at 2073 K (1800 °C) were determined in the compositional range of 65 or 70 at. pct Mo, 1.7 to 6.7 at. pct Si, 3.3 to 13.3 at. pct B, 7.5 to 15.0 or 5.0 to 12.5 at. pct Ti, and 7.5 to 15.0 or 5.0 to 12.5 at. pct C in the Mo-Ti-Si-C-B five-element system. Furthermore, compression tests were carried out for the heat-treated alloys at 1673 K (1400 °C). The high-temperature strength of the TiC-added Mo-Si-B alloys is discussed in terms of the microstructure and volume fraction of the constituent phases.

II. MATERIALS AND PROCEDURES

Eight TiC-added Mo-Si-B alloys, divided into two series, were prepared by a conventional arc-melting technique in Ar atmosphere. In series A, the Mo concentration was fixed at 65 at. pct, and while keeping the Si:B ratio at 1:2, the TiC concentration was varied from 15.0 at. pct (A_1), *i.e.*, 15.0 at. pct Ti and 15.0 at. pct C, to 12.5 at. pct (A_2), 10.0 at. pct (A_3), and 7.5 at. pct (A_4). In series B, the Mo concentration was constant at 70 at. pct. Keeping the Si:B ratio at 1:2 in the same manner as those alloys in series A, the TiC concentration was varied from 12.5 at. pct (B_1) to 10.0 at. pct (B_2), 7.5 at. pct (B_3), and 5 at. pct (B_4). These weighed compositions are tabulated in Table I and also expressed schematically in the Mo-Mo_5SiB_2-TiC pseudo-ternary triangle shown in Figure 2. Button ingots of approximately 15 g in weight were cast by melting together pure Mo (99.99 wt. pct), Si (99.9999 wt. pct), B (99.95 wt. pct), and cold-pressed TiC powder (99 wt. pct, 2 to 5 μm in diameter). Each alloy ingot was flipped and remelted 5 times to insure maximum compositional homogeneity. Prior to each melting, the furnace was evacuated and filled several times with high-purity Ar gas, and a pure Ti ingot was melted before every melting to remove residual O_2 and N_2 gases. There was little difference (≤0.1 wt. pct loss) in the alloy weight before and after melting.

Table I. Weighed Compositions of the TiC-Added Mo-Si-B Alloys

	Composition (at. pct)				
	Mo	Si	B	Ti	C
A_1	65.0	1.7	3.3	15.0	15.0
A_2	65.0	3.3	6.7	12.5	12.5
A_3	65.0	5.0	10.0	10.0	10.0
A_4	65.0	6.7	13.3	7.5	7.5
B_1	70.0	1.7	3.3	12.5	12.5
B_2	70.0	3.3	6.7	10.0	10.0
B_3	70.0	5.0	10.0	7.5	7.5
B_4	70.0	6.7	13.3	5.0	5.0

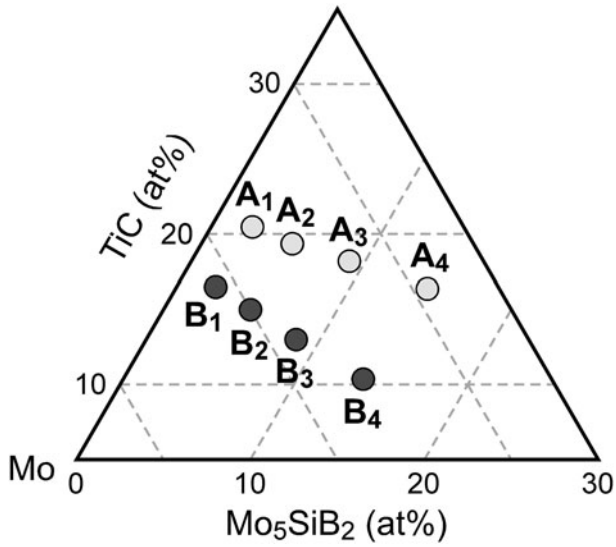

Fig. 2—Compositional variation of the series A and B alloys in a Mo-Mo_5SiB_2-TiC pseudo-ternary triangle.

Heat treatment was carried out for all ingots at 2073 K (1800 °C) for 24 hours also in Ar atmosphere. Constituent phases were identified by X-ray diffractometry (XRD; Bruker D8 Advance) using Cu Kα radiation. Microstructures were observed by scanning electron microscopy (SEM; JEOL JSM-6500F and Philips XL-30FEG) *via* back-scattered electron (BSE) images and by transmission electron microscopy (TEM; JEOL JEM-2100). Thin foils for the TEM observation were prepared by a focused ion beam (FIB) technique (JEOL JIB-4600F) using a Ga ion beam at 30 kV. Semi-quantitative composition analyses of the constituent phases were performed by energy dispersive X-ray spectroscopy (EDX) in both SEM and TEM. The alloy densities were measured at room temperature using Archimedes' principle. Compression specimens with a size of about 2 × 2 × 4 mm^3 were cut from the center of the ingots after heat treatment by electro-discharge machining (EDM), and tests were conducted at 1673 K (1400 °C) in a vacuum of better than 10^{-3} Pa using an

Instron 8862 machine equipped with a vacuum furnace and W-mesh heaters. The actuator speed was constant at 0.05 mm/min corresponding to an initial strain rate of 2×10^{-4} s^{-1}. For each test, the specimen was sandwiched between SiC plates, 15 × 15 × 5 mm in size, to reduce the stress concentration at the surfaces of the W push rods. For a comparison of the density and high-temperature strength, an as-received alloy of Mo-(1.0-1.3 wt. pct)Hf-(0.05 to 0.12 wt. pct)C (MHC) produced by Plansee SE was employed in this study.

III. RESULTS

A. *As-Cast Microstructures*

Figure 3 shows the XRD profiles of the as-cast series A and B samples. In this study, ideal X-ray intensities were not obtained since bulk samples were used for XRD. Qualitatively speaking, as shown in Figure 3(a), the Mo_{ss} and TiC peaks of alloy A_1 are relatively strong and there are low-intensity peaks of T_2. With increasing Si and B content keeping the Si-to-B ratio to 1/2 and decreasing TiC content in alloys A_1 to A_4, the T_2 peaks increased in intensity. In A_3 and A_4, the Mo_2C peaks are distinct, suggesting that the volume fraction of Mo_2C somehow increased with an increase in the Si and B and a decrease in the TiC content. In contrast, the TiC peaks are extremely weak in alloy A_4, suggesting that the volume fraction of TiC drastically decreased in the alloy. For the series B alloys, the peaks of the four phases, *i.e.*, Mo_{ss}, T_2, TiC, and Mo_2C, are also detected as shown in Figure 3(b). In a similar manner to the results seen for series A, the TiC peaks became weaker and those of T_2 and Mo_2C became stronger with increasing Si and B and deceasing TiC content. These results indicate that the constituent phases of both the series A and B alloys are Mo_{ss}, T_2, TiC, and Mo_2C and that their volume fraction varies depending on the relative Si and B and TiC contents.

As-cast microstructures of the series A alloys are shown in Figure 4, and as expected from the XRD profiles, the as-cast microstructure changes with composition. In alloy A_1 (Figure 4(a)), almost the whole area is composed of primary TiC and a Mo_{ss} + TiC eutectic as the secondary phase where fine and elongated TiC (black phase) is embedded in the Mo_{ss} (white phase). Between the primary TiC and Mo_{ss} + TiC eutectic areas, there are two more eutectics: Mo_{ss} + T_2 + TiC and Mo_{ss} + T_2 + Mo_2C. (The constituent phases were characterized by TEM-EDX as described later in addition to XRD and SEM-EDX.) The fine microstructure of these eutectics is on the submicrometer scale and the volume fractions are much smaller than that of the primary TiC and secondary Mo_{ss} + TiC eutectic. This is reason for the low intensity of the Mo_2C peaks in the XRD profile of alloy A_1. The volume fractions of the primary TiC and secondary Mo_{ss} + TiC eutectic in alloy A_2 are smaller than those in A_1 as shown in Figure 4(b). Between the primary TiC and Mo_{ss} + TiC eutectic areas, there are fragments of T_2 in addition to the Mo_{ss} + T_2 + TiC and Mo_{ss} + T_2 + Mo_2C eutectics,

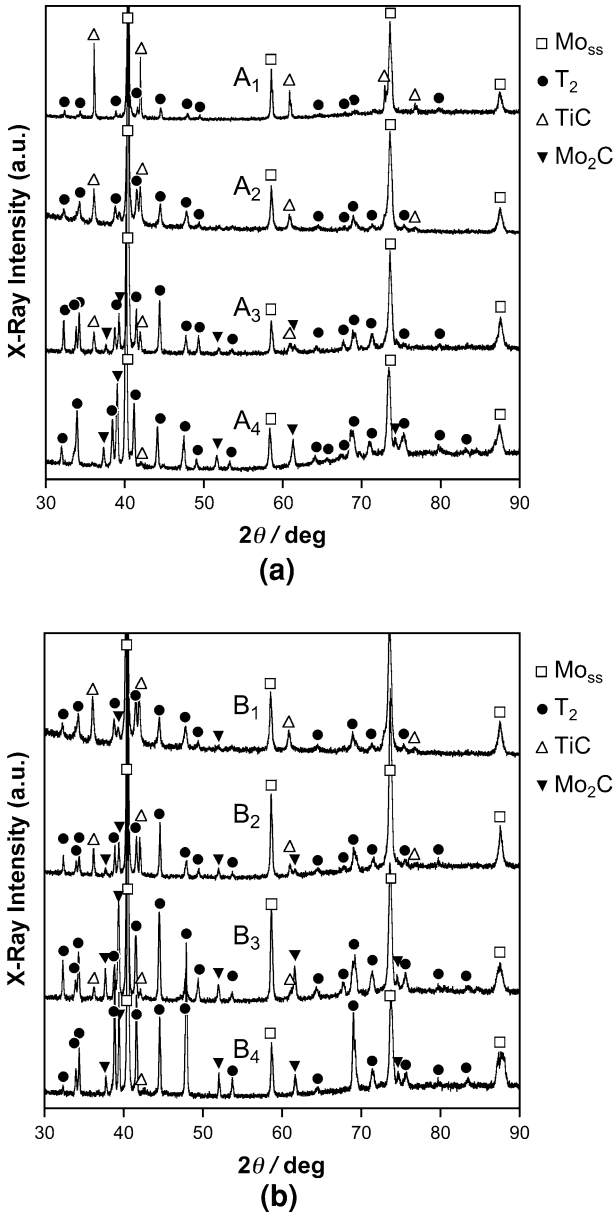

Fig. 3—XRD profiles of the as-cast TiC-added Mo-Si-B alloys. (*a*) Series A alloys. (*b*) Series B alloys.

which suggest that T_2 is the tertiary phase to be solidified from liquid. In alloy A_2, the microstructure fineness of the Mo_{ss} + T_2 + Mo_2C eutectic is on the micrometer scale, which is coarser than that of the Mo_{ss} + T_2 + TiC eutectic, which is still on the submicrometer scale. In alloy A_3 (Figure 4(c)), the volume fractions of the primary TiC and secondary Mo_{ss} + TiC eutectic are considerably smaller than those in A_1 and A_2, and colony structures consisting of the Mo_{ss} + T_2 + TiC and Mo_{ss} + T_2 + Mo_2C eutectics are observed, with fragments of the tertiary T_2 between the primary and secondary eutectic areas. The colony boundaries are formed from the Mo_{ss} + T_2 + Mo_2C eutectic, while the colony interiors consist of the Mo_{ss} + T_2 + TiC eutectic. The microstructure fineness of the colony boundaries is on the micrometer scale,

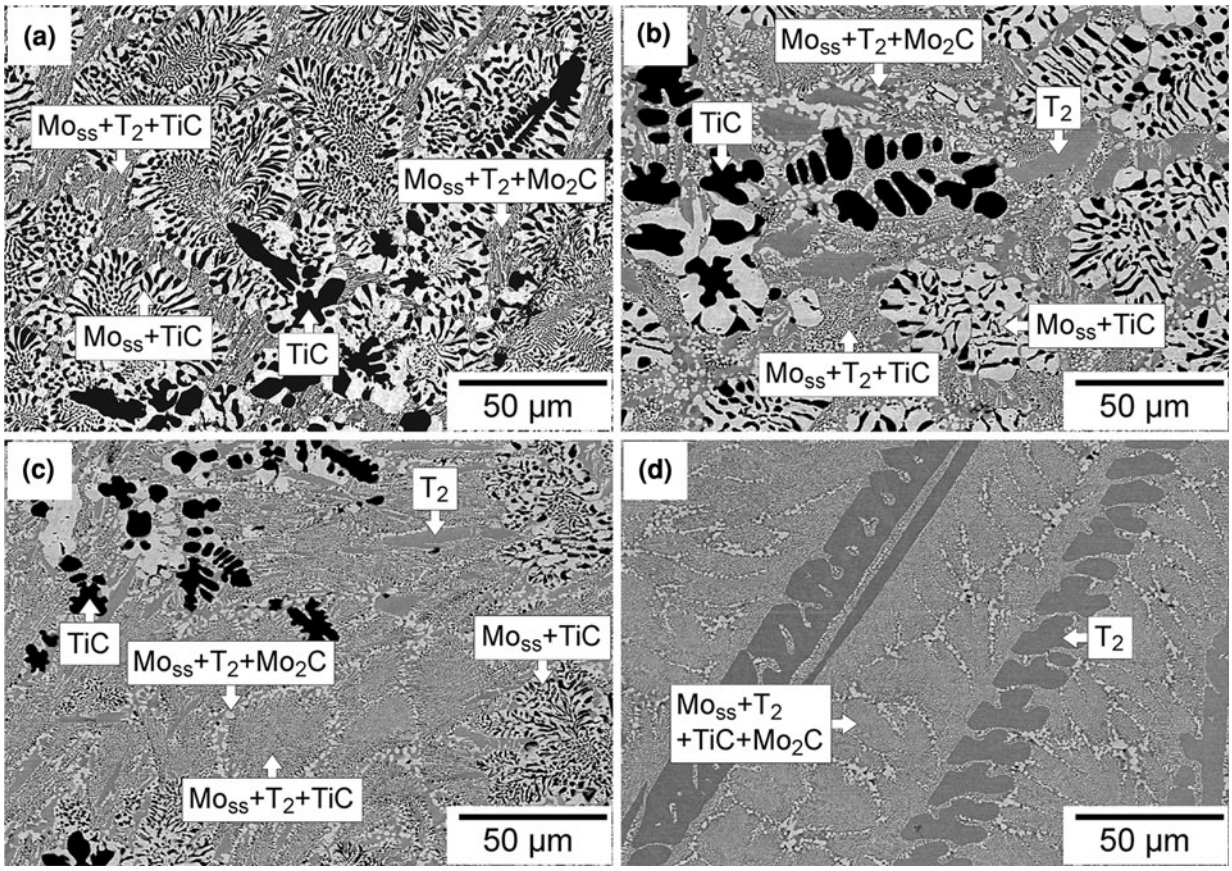

Fig. 4—BSE images of the as-cast microstructures of the series A alloys. (*a*) A_1, (*b*) A_2, (*c*) A_3, and (*d*) A_4.

similar to the case in A_2, and coarser than the submicrometer-scale colony interiors. The microstructure of alloy A_4 is considerably different from the others as shown in Figure 4(d). The primary phase of A_4 is T_2, and there are colony structures between the elongated T_2 dendrites. However, neither the colony interiors nor boundaries are composed of the $Mo_{ss} + T_2 + TiC$ eutectic or the $Mo_{ss} + T_2 + Mo_2C$ eutectic, but of a $Mo_{ss} + T_2 + TiC + Mo_2C$ four-phase eutectic. The absence of the primary TiC and $Mo_{ss} + TiC$ eutectic induces a significant decrease in the TiC volume, which is consistent with the low-intensity TiC peaks in the XRD profile of A_4.

As-cast microstructures of the series B alloys are shown in Figure 5. The primary phase in alloy B_1 is Mo_{ss}, which has a dendritic shape as shown in Figure 5(a), and a large volume of the secondary $Mo_{ss} + TiC$ eutectic is also present. Between the primary Mo_{ss} and secondary $Mo_{ss} + TiC$ eutectic, there are fine eutectic areas consisting of the $Mo_{ss} + T_2 + TiC$ and $Mo_{ss} + T_2 + Mo_2C$ eutectics with a microstructure fineness on the submicrometer scale. In alloy B_2 (Figure 5(b)), the primary Mo_{ss} became coarser and globular. The secondary $Mo_{ss} + TiC$, tertiary T_2, and $Mo_{ss} + T_2 + TiC$ and $Mo_{ss} + T_2 + Mo_2C$ eutectics are between the primary Mo_{ss}. The volume fraction of the secondary $Mo_{ss} + TiC$ appears to decrease in comparison with that in B_1, suggesting that the composition of B_2 is located further inside the primary Mo_{ss} area and away from the $Mo_{ss} + TiC$ eutectic line. The dendritic primary phase of Mo_{ss} is also present in alloy B_3, as shown in Figure 5(c), but the $Mo_{ss} + TiC$ eutectic has completely disappeared. The areas between the primary Mo_{ss} are entirely composed of the colony-structured $Mo_{ss} + T_2 + TiC + Mo_2C$ four-phase eutectic in a similar manner to that observed in A_4, where the microstructure fineness was also on the submicrometer scale. Furthermore, in alloy B_4 (Figure 5(d)), the primary Mo_{ss} completely disappeared, but there are still some fragments of T_2, suggesting that this is the primary phase of B_4. However, the volume fraction of the T_2 is very small, and almost all areas are composed of a slightly coarser $Mo_{ss} + T_2$ eutectic and a finer $Mo_{ss} + T_2 + Mo_2C$ eutectic. The presence of TiC in B_4 was not confirmed by SEM.

To confirm the phase constitutions of the eutectics and that the microstructure fineness is on the submicrometer scale, the $Mo_{ss} + T_2 + TiC$ and $Mo_{ss} + T_2 + TiC + Mo_2C$ eutectics were observed and characterized by TEM. An example TEM micrograph of the $Mo_{ss} + T_2 + TiC$ eutectic in the interior of a colony in A_3 is shown in Figure 6(a). Diffraction patterns and EDX spectra taken from the locations indicated by the symbols in the bright-field image were analyzed as shown in Figure 6(b) through (d). The results confirm that the colony interior is composed of Mo_{ss}, T_2, and TiC in the form of a $Mo_{ss} + T_2 + TiC$ three-phase eutectic. Figure 7(a) shows a TEM micrograph of the

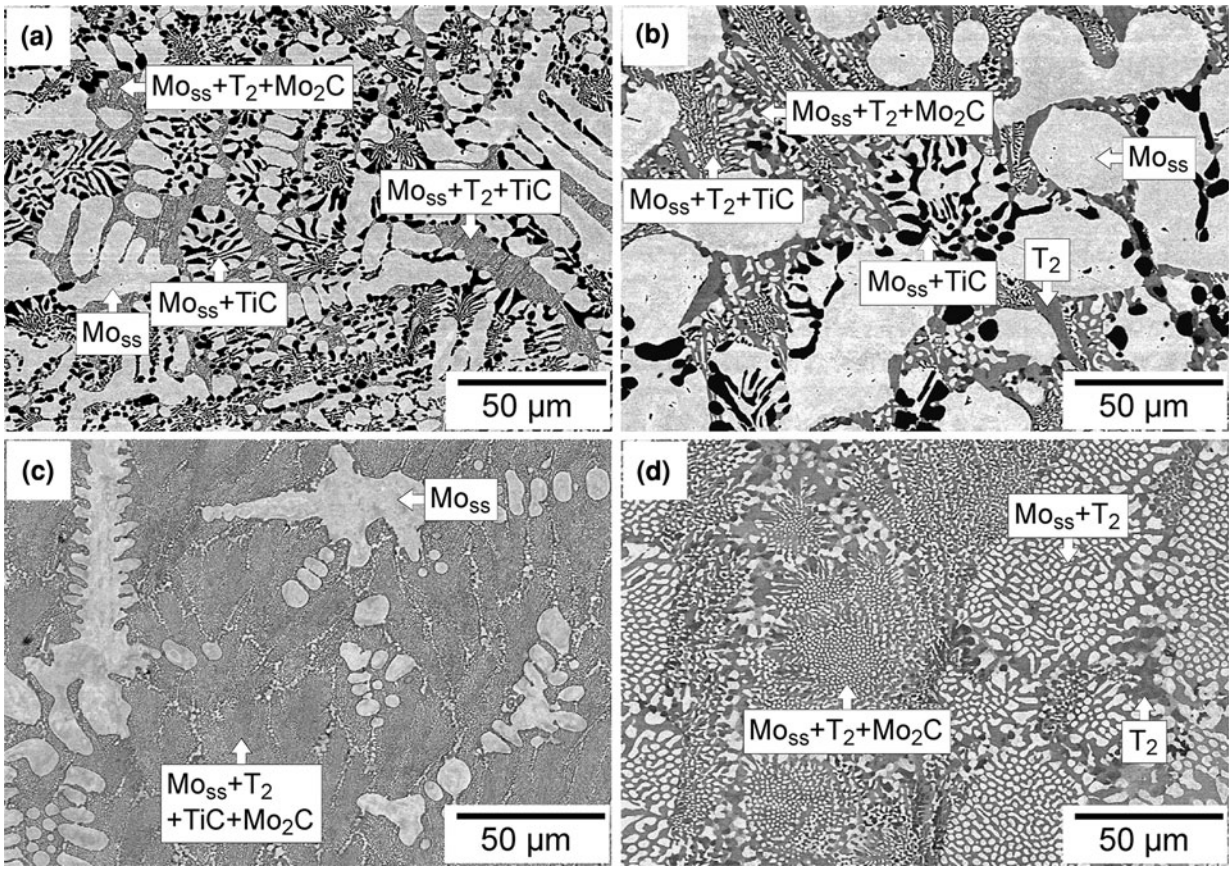

Fig. 5—BSE images of the as-cast microstructures of the series B alloys. (*a*) B_1, (*b*) B_2, (*c*) B_3, and (*d*) B_4.

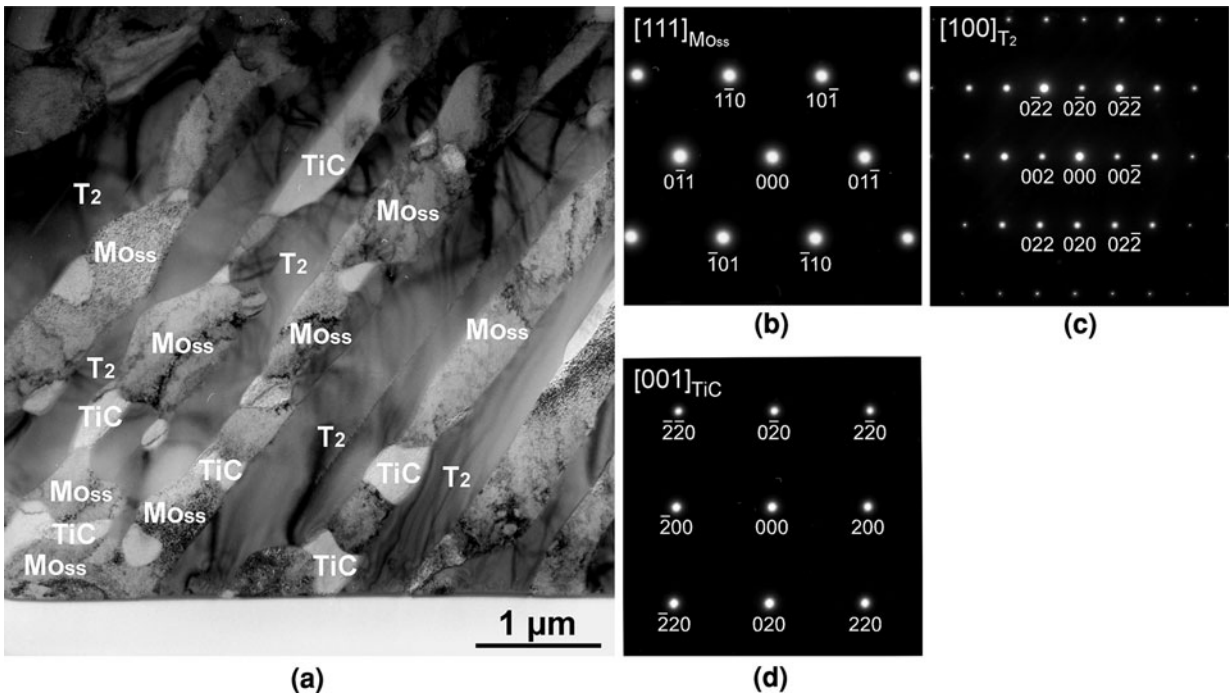

Fig. 6—(*a*) Bright-field transmission electron micrograph of a colony interior of alloy A_3. Diffraction patterns from the (*b*) [111] direction of Mo_{ss}, (*c*) [100] direction of T_2, and (*d*) [001] direction of TiC.

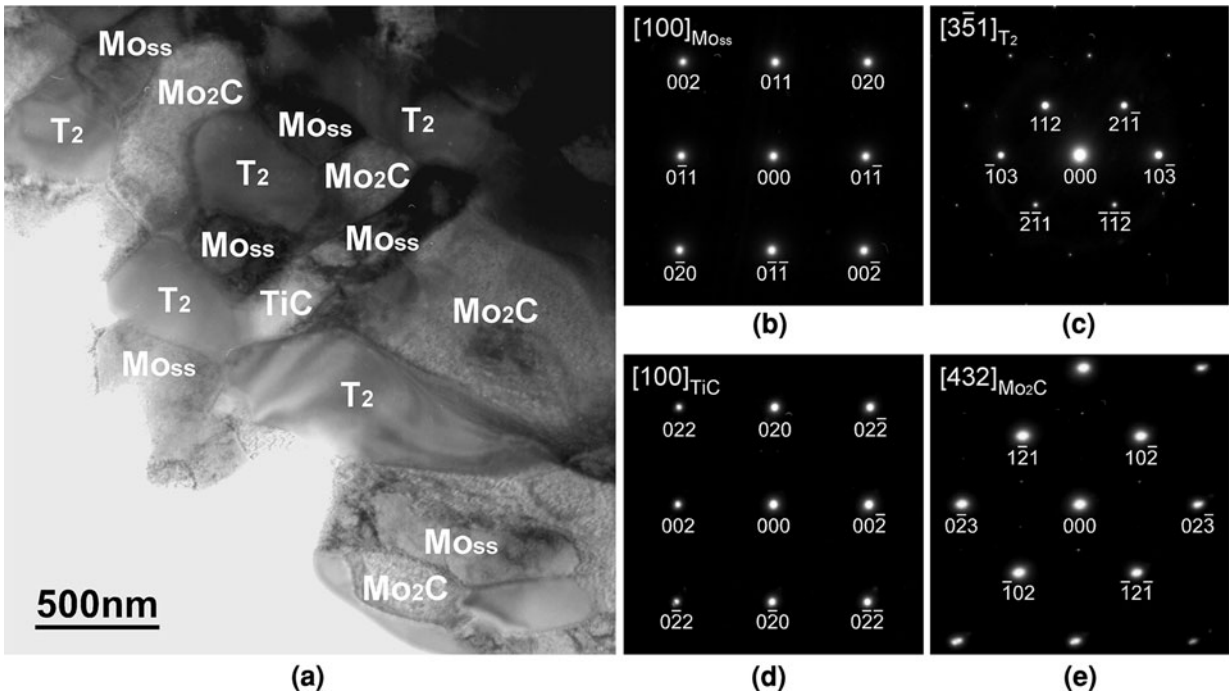

Fig. 7—(*a*) Bright-field transmission electron micrograph of a colony interior of alloy B_3. Diffraction patterns from the (*b*) [100] direction of Mo_{ss}, (*c*) $3\bar{5}1$ direction of T_2, (*d*) [100] direction of TiC, and (*e*) [432] direction of Mo_2C.

$Mo_{ss} + T_2 + TiC + Mo_2C$ in the interior of a colony in B_3. Diffraction patterns (Figures 7(b) and (c)) and EDX spectra again confirm that the colony interior is composed of Mo_{ss}, T_2, TiC and Mo_2C.

B. *Microstructures After Heat Treatment at 2073 K (1800 °C) for 24 hours*

During the heat treatment at 2073 K (1800 °C) for 24 hours, the microstructure changed in all the alloys and coarsening took place particularly in the $Mo_{ss} + T_2 + TiC$, $Mo_{ss} + T_2 + Mo_2C$, and $Mo_{ss} + T_2 + TiC + Mo_2C$ eutectic areas. In alloy A_1 (Figure 8(a)), the primary TiC remains almost the same size and shape, but the TiC in the $Mo_{ss} + TiC$ eutectic areas is spheroidized. The sample is almost entirely composed of Mo_{ss} and TiC two-phase areas, with equiaxed T_2 distributed between the two-phase areas. Very little Mo_2C was observed in the annealed A_1. In the annealed A_2, the volume fraction of the Mo_{ss} and TiC two-phase areas is smaller than that in A_1, in a similar manner to the as-cast microstructure, and irregularly shaped T_2 fills the space between the two-phase areas as shown in Figure 8(b). As a result, the volume fraction of T_2 in A_2 is higher than that in A_1. In the annealed A_3, the volume fraction of the Mo_{ss} and TiC two-phase area is considerably small, and dendritic-shaped areas consisting of T_2 and Mo_2C surrounded by Mo_{ss} are remarkably developed (Figure 8(c)). Small precipitates are found in the relatively coarse and dendritic-shaped T_2 areas. Careful observation demonstrates that some areas where the T_2 and TiC are homogeneously distributed in a Mo_{ss} matrix are also widely developed between the dendritic-shaped areas. The constitutional phases in the dendritic-shaped areas are Mo_{ss}, T_2, and Mo_2C, while those in the Mo_{ss} matrix are Mo_{ss}, T_2, and TiC. These constitutional phases suggest that the dendritic-shaped areas developed from the colony boundaries and that the Mo_{ss} matrix areas developed from the colony interiors seen in the as-cast microstructure. The microstructure fineness of the dendritic-shaped areas is in the order of several micrometers and that of the Mo_{ss} matrix areas is in the micrometer scale. This means that these areas underwent a tenfold increase in the coarseness during heat treatment. In the annealed A_4 (Figure 8(d)), the dendritic primary T_2 remains with little change in the shape or size and contains a large amount of small precipitates. The equiaxed $Mo_{ss} + T_2 + TiC + Mo_2C$ four-phase areas are uniformly evolved on the micrometer scale between the primary T_2 dendrites, also indicating an almost tenfold increase in the microstructure fineness of the $Mo_{ss} + T_2 + TiC + Mo_2C$ eutectic during heat treatment. It is worth noting that TiC exists within or at the interfaces with Mo_{ss}, but that it is scarce in the T_2 and Mo_2C in the homogenous microstructure areas. Mo_{ss} may play a role in the nucleation and/or growth of TiC in the system.

In the annealed B_1 and B_2 alloys (Figures 9(a) and (b)), the primary Mo_{ss} retains its shape and size, and the TiC is spheroidized. T_2 is predominantly developed between the Mo_{ss} and TiC areas. The primary Mo_{ss} and relatively coarse T_2 contain fine precipitates. The presence of Mo_2C in B_1 and B_2 was not confirmed by SEM. In the annealed B_3, microstructure coarsening occurred in the $Mo_{ss} + T_2 + TiC + Mo_2C$ eutectic areas as shown in Figure 9(c). Again, TiC exists within or at the interfaces with Mo_{ss}, but is scarce in the T_2 and Mo_2C. It should be noted that the boundaries of the

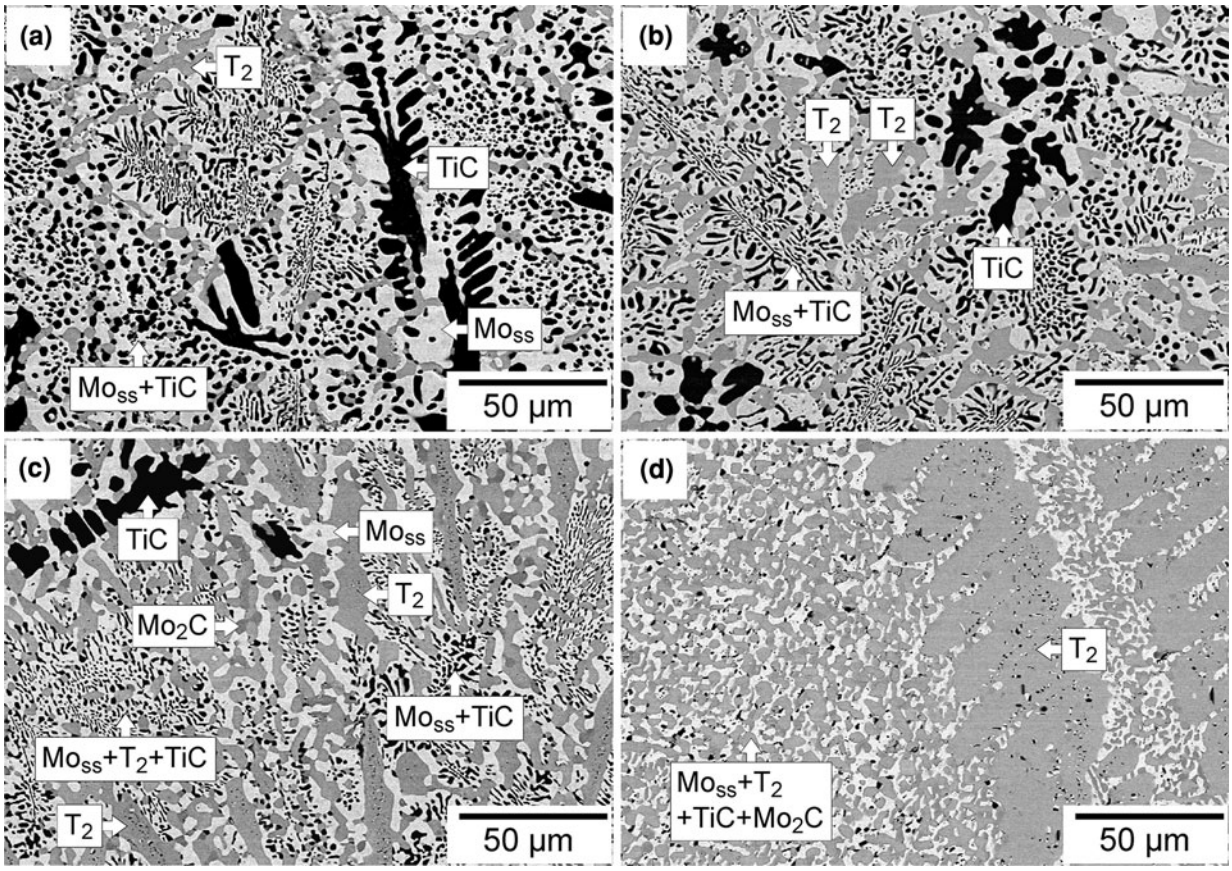

Fig. 8—BSE images of the microstructures of the series A alloys after heat treatment at 2073 K (1800 °C) for 24 h. (*a*) A_1, (*b*) A_2, (*c*) A_3, and (*d*) A_4.

primary Mo_{ss} areas appear to be preferentially pinned by TiC particles. TiC may prevent interfacial boundary migration and improve the microstructure stability in the alloys. Indeed, the microstructural evolution and coarsening developed drastically in alloy B_4, which has no TiC, as shown in Figure 9(d). In the alloy, equiaxed Mo_{ss}, T_2, and Mo_2C are homogeneously distributed on a 10-μm scale.

Figure 10(a) shows the interior of a coarse and dendritic T_2 area in the annealed A_3 (Figure 8(c)). As mentioned above, the primary or tertiary solidified coarse T_2 contains a large amount of small precipitates. As shown in Figure 10(a), these precipitates consist of Mo_{ss}, TiC, and Mo_2C. This evidence indicates that the as-cast T_2 contains an amount of supersaturated Mo, Ti, and C. It is interesting that Mo_{ss} and TiC combine even within T_2. Figure 10(b) shows the interior of a primary Mo_{ss} area in the annealed B_3 alloy (Figure 9(c)): Plate-like TiC precipitates within the primary Mo_{ss} can be seen. This indicates that the as-cast primary Mo_{ss} contains an amount of supersaturated Ti and C. No other phases such as Mo_2B, MoB, Mo_3Si, or Mo_5Si_3 were observed as precipitates.

The volume fractions of the constituent phases in the series A and B alloys were measured from an image analysis of the BSE contrast obtained after the heat treatment. The results are shown in Figure 11. The volume fraction data of T_2 and Mo_2C are combined in this figure because it was difficult to separate these two phases in the SEM-BSE images due to their weak contrast difference. In the series A alloys, the volume fractions of Mo_{ss} and TiC decrease and that of $T_2 + Mo_2C$ increases as the composition changes from that of A_1 to A_4, as shown in Figure 11(a). The Mo_{ss} volume fractions in the series A alloys are relatively high in spite of the TiC primary. A_1 has a Mo_{ss} volume fraction of over 60 pct, A_2 of over 50 pct, and A_3 of approximately 46 pct. In contrast, the Mo_{ss} volume fractions in the series B are not as high despite the Mo_{ss} primary, as shown in Figure 11(b). There is a tendency for the volume fraction of $T_2 + Mo_2C$ to increase with decreasing volume fraction of TiC in both the series A and B alloys.

C. *Compressive Strength at 1673 K (1400 °C)*

Stress–strain curves obtained from compression tests at 1673 K (1400 °C) are shown in Figure 12. For comparison, the stress–strain curve of MHC obtained under the same conditions is also shown. As shown in Figure 12(a), alloy A_1 began to yield at around 200 MPa, followed by work hardening, and transferred to almost constant flow behavior at a plastic strain of around 4 pct. The 0.2 pct proof stress was approximately 350 MPa. The onset stresses of yielding were almost the same for the other series A alloys.

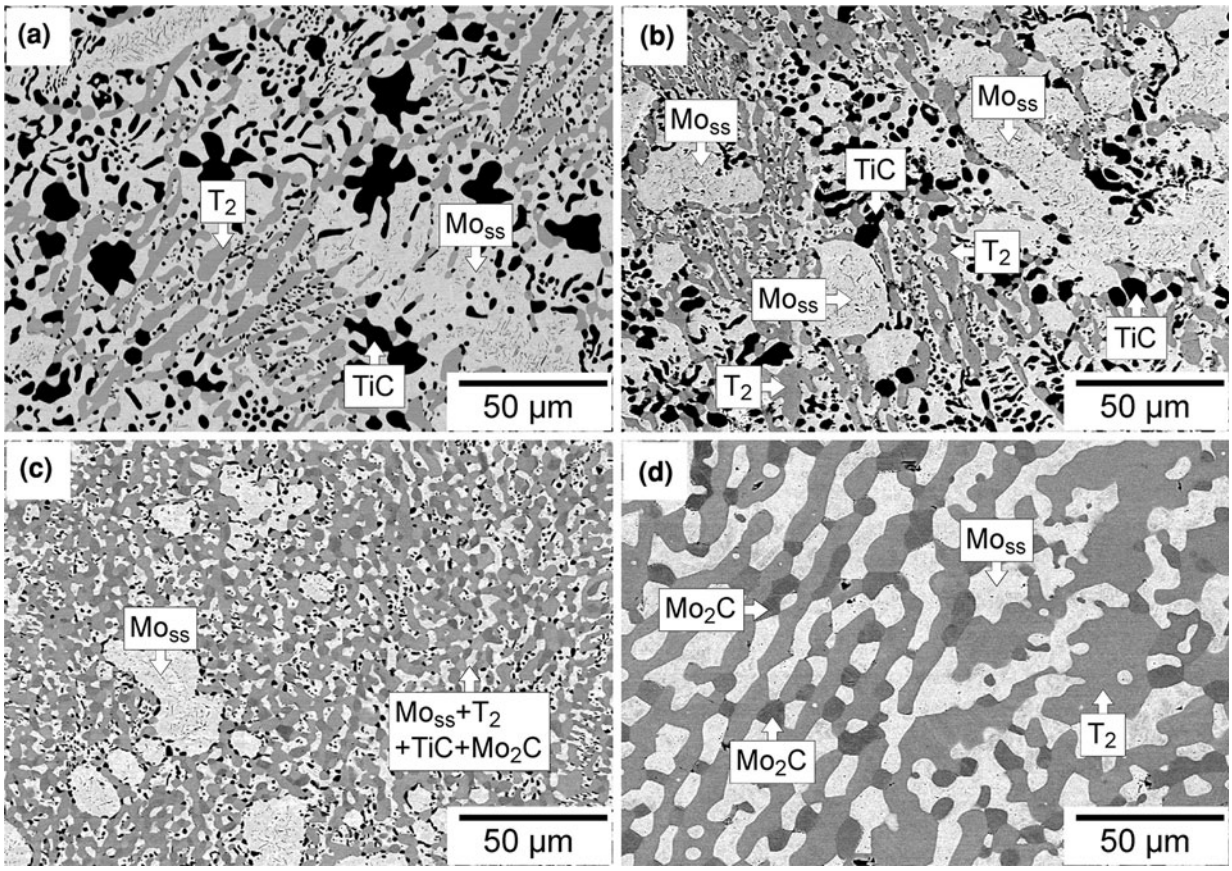

Fig. 9—BSE images of the microstructures of the series B alloys after heat treatment at 2073 K (1800 °C) for 24 h. (*a*) B_1, (*b*) B_2, (*c*) B_3, and (*d*) B_4.

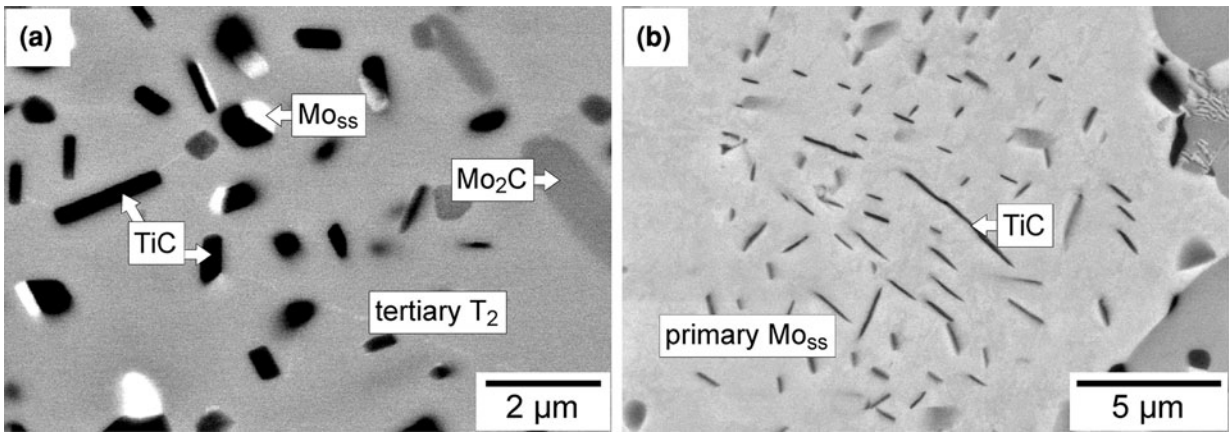

Fig. 10—BSE images at high magnification for (*a*) tertiary T_2 in alloy A_3 and (*b*) primary Mo_{ss} in alloy B_3.

The work-hardening rate gradually increased as the composition changed from alloy A_1 to A_4: The stress–strain curves place the ultimate compressive strength (UCS) at around a 3 to 4 pct plastic strain for alloys A_2 to A_4. Consequently, the UCS increased as the composition changed from that of A_2 to A_4 and was extremely high, over 1 GPa, for A_4. The flow stresses of A_2 and A_3 decreased gradually, while that of A_4 decreased rapidly after the UCS. The MHC alloy also showed an onset stress of yielding at around 200 MPa. However, the 0.2 pct proof stress and constant flow stress are 300 and 350 MPa, respectively, which are much lower than the series A alloys.

For the series B alloys, as shown in Figure 12(b), the onset stress of yielding depends on the alloy composition, and as a result, the 0.2 pct proof stress also varies among the alloys. The onset stress of yielding and 0.2 pct proof stress of B_1 are almost the same as those of

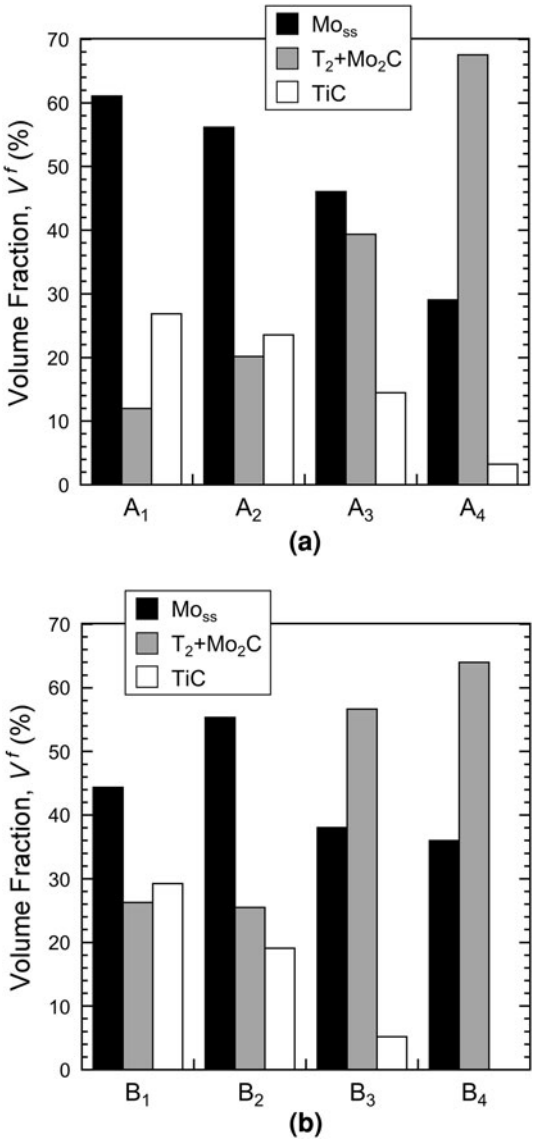

Fig. 11—Volume fractions of Mo_{ss}, T_2 + Mo_2C, and TiC measured by image analysis for (*a*) series A alloys and (*b*) series B alloys.

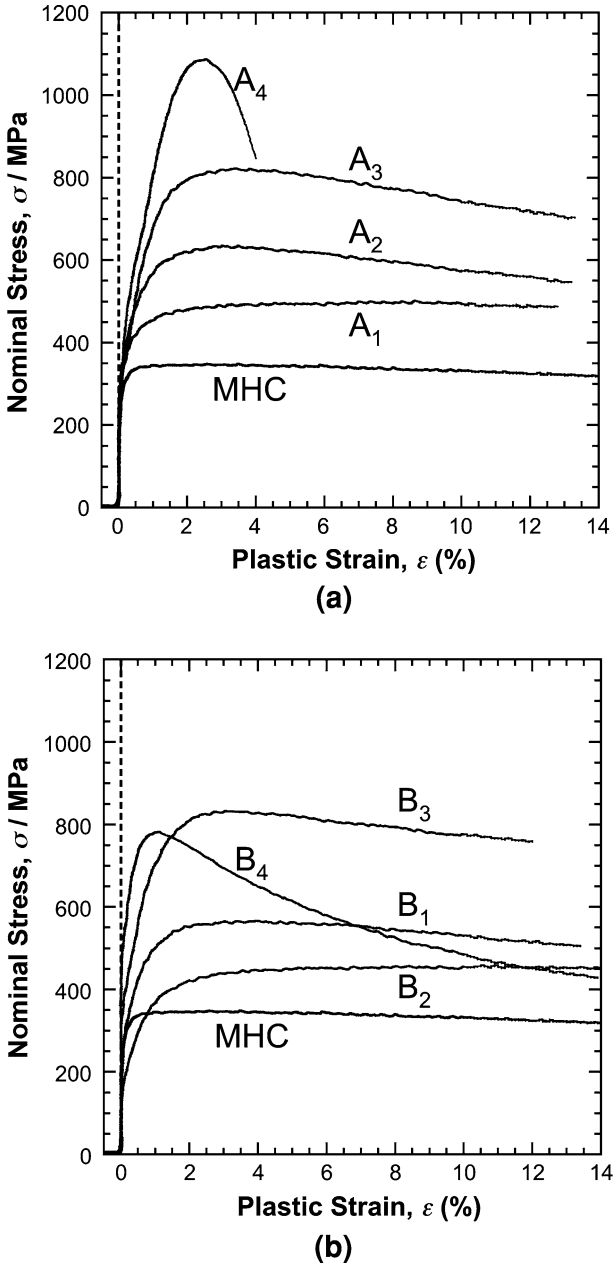

Fig. 12—Nominal stress *vs.* plastic strain curves obtained by compression tests at 1673 K (1400 °C) and a strain rate of 2×10^{-4} s^{-1}. (*a*) Series A and (*b*) series B alloys with MHC.

the MHC, but those of B_2 are lower than those of the MHC. The onset stress of yielding and 0.2 pct proof stress of B_3 and B_4 are higher than those of B_1 and the MHC. The stress–strain curves show that B_1 and B_2 transferred to constant flow behavior after work hardening. In contrast, those of B_3 and B_4 show that the UCS is followed by flow stress-lowering behavior. While B_1, B_2, and B_3 had constant flow stresses or UCSs at around a 3 to 4 pct plastic strain, a drop in the flow stress occurred for less than 1 pct plastic strain in B_4.

The densities of the series A and B alloys after the heat treatment are shown in Figure 13 and compared with those of pure Ni, pure Mo,[20] T_2,[8] MHC, and some representative Ni-base single-crystal (SX) superalloys.[16] The series A and B alloys have densities of approximately 8.70 to 9.01 g/cm^3, which are comparable to that of monolithic T_2, 8.86 g/cm^3, and within the Ni-base superalloy density range. Therefore, the addition of TiC brings about the formation of $Mo_{ss}/T_2/TiC/Mo_2C$ in the Mo-Si-B alloys and works to lower the density to that of Ni-base superalloys. The 0.2 pct proof stresses and UCSs obtained from Figure 12 are converted into specific values by dividing by the density data: The values are shown in Figure 14. Almost all the 0.2 pct proof stresses except that of B2 are in excess of the MHC value, and all the UCSs (or constant flow stresses) are higher than that of the MHC. For the series A alloys, the UCS increased monotonically as the composition changed from that of alloy A_1 to A_4. The UCS of A_2 is about twice as high as the constant flow

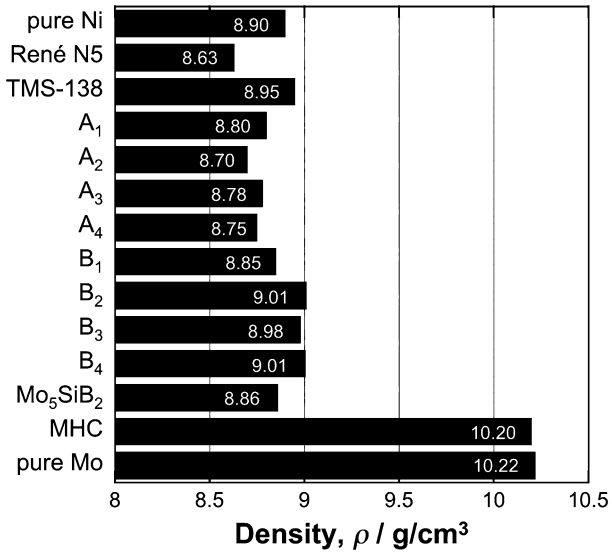

Fig. 13—Densities of the series A and B alloys measured using Archimedes' principle at room temperature, compared with those of pure Ni, pure Mo,[20] T_2,[8] MHC, and some representative Ni-base single-crystal (SX) superalloys.[16]

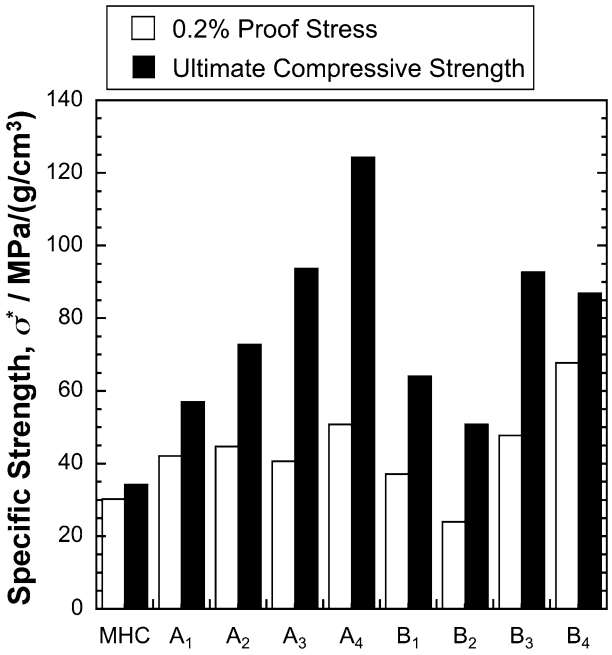

Fig. 14—Specific 0.2 pct proof stress and ultimate compressive strength of the series A and B alloys.

stress of the MHC, and those of A_3 and A_4 are three and four times larger, respectively. The UCSs of the series B alloys varied with their 0.2 pct proof stresses, and the UCS of B_4 is relatively low compared with that of B_3 because of the premature drop in the flow stress.

Figure 15 shows an SEM-BSE micrograph of alloy A_4 after deformation. As can be seen, microcracking occurred within the T_2 phase, but not in any other phases. This microcracking within the T_2 to a greater or lesser extent was also observed in the other alloys, which suggests that microcracking is responsible for the flow

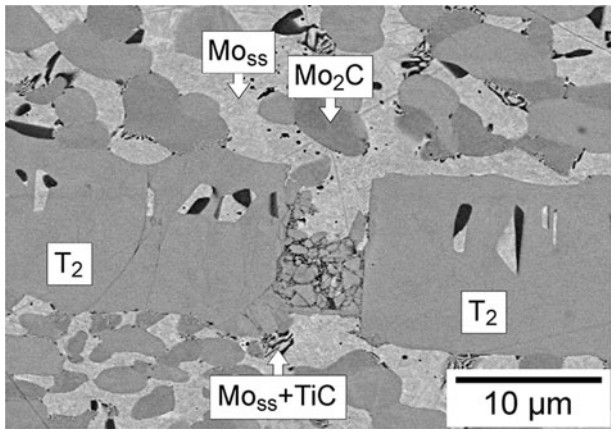

Fig. 15—BSE image of the microstructure of alloy A_4 after a compression test at 1673 K (1400 °C).

stress-lowering behavior. In other words, TiC and Mo_2C exhibited good deformability at a temperature of 1673 K (1400 °C) and a strain rate of 2×10^{-4} s^{-1}. The volume fraction of $T_2 + Mo_2C$ in alloy A_4 is the highest and followed by that in B_4 (Figure 11). It is expected from these results that the volume fraction of T_2 is higher in alloys A_4 and B_4, and this is a reasonable expectation from the compositional variation shown in Figure 2. Furthermore, alloy A_4 has coarse and dendritic T_2 since the T_2 is the primary phase. Therefore, the drastic drop in the flow stress of both A_4 and B_4 observed in Figure 12 is considered to be caused by microcracking of the T_2 phase.

IV. DISCUSSION

In the TiC-added Mo-Si-B alloys, the four phases, *i.e.*, Mo_{ss}, T_2, TiC, and Mo_2C, are crystallized out during solidification. The primary phases of A_1, A_2, and A_3 were TiC, and T_2 crystallization was observed in alloys A_2 and A_3. It has been reported that the melting point of T_2 is about 2473 K (2200 °C) near or at the stoichiometric composition, while it is significantly lower for nonstoichiometric compositions.[4,5] As shown in Figure 10(c), the crystallized T_2 contained a large amount of supersaturated Mo_{ss}, Ti, and C, suggesting that the melting point of the T_2 crystallized out in alloys A_2 and A_3 is lower than 2473 K (2200 °C) and also lower than the reaction temperature of 2448 K (2175 °C) for the $Mo_{ss} + TiC$ eutectic (Figure 1).[18] Thus, the secondary phase of alloys A_1, A_2, and A_3 would be the $Mo_{ss} + TiC$ eutectic, and the tertiary phase of A_2 and A_3 would be T_2. Alloy A_3 has colony structures of $Mo_{ss} + T_2 + TiC$ and $Mo_{ss} + T_2 + Mo_2C$. Since the colony interiors consist of $Mo_{ss} + T_2 + TiC$ and the colony boundaries of $Mo_{ss} + T_2 + Mo_2C$, the eutectic reaction of $Mo_{ss} + T_2 + TiC$ would be followed by the reaction of $Mo_{ss} + T_2 + Mo_2C$. For A_4, it is clear that the primary and secondary phases are T_2 and the $Mo_{ss} + T_2 + TiC + Mo_2C$ eutectic, respectively. The primary phase of B_1, B_2, and B_3 is Mo_{ss}. Based on the

same argument, the secondary phase of B_1 and B_2 is the Mo_{ss} + TiC eutectic, the tertiary phase of B_2 is T_2 followed by the Mo_{ss} + T_2 + TiC and Mo_{ss} + T_2 + Mo_2C eutectics. The secondary phase of B_3 is simply the Mo_{ss} + T_2 + TiC + Mo_2C eutectic. In B_4, the primary phase was determined to be T_2, although its volume fraction was noted to be very small. It is not clear in the present study if the reaction temperature of the Mo_{ss} + T_2 eutectic or the Mo_{ss} + T_2 + Mo_2C eutectic is higher. However, since the Mo_{ss} + T_2 + Mo_2C eutectic had colony structures and the colony boundaries were coarser than the colony interiors, it is suggested that solidification was completed at the Mo_{ss} + T_2 + Mo_2C colony boundaries. Hence, for B_4, the secondary phase is considered to be the Mo_{ss} + T_2 eutectic and the tertiary phase to be the Mo_{ss} + T_2 + Mo_2C eutectic. Thus, the solidification pathways of the series A and B alloys can be summarized as follows:

Alloy A_1: TiC (primary) → Mo_{ss} + TiC eutectic (secondary) → Mo_{ss} + T_2 + TiC eutectic (tertiary) → Mo_{ss} + T_2 + Mo_2C eutectic (quaternary).
Alloys A_2 and A_3: TiC (primary) → Mo_{ss} + TiC eutectic (secondary) → T2 (tertiary) → Mo_{ss} + T_2 + TiC eutectic (quaternary) → Mo_{ss} + T_2 + Mo_2C eutectic (quinary).
Alloy A_4: T_2 (primary) → Mo_{ss} + T_2 + TiC + Mo_2C eutectic (secondary).
Alloy B_1: Mo_{ss} (primary) → Mo_{ss} + TiC eutectic (secondary) → Mo_{ss} + T_2 + TiC eutectic (tertiary) → Mo_{ss} + T_2 + Mo_2C eutectic (quaternary).
Alloy B_2: Mo_{ss} (primary) → Mo_{ss} + TiC eutectic (secondary) → T2 (tertiary) → Mo_{ss} + T_2 + TiC eutectic (quaternary) → Mo_{ss} + T_2 + Mo_2C eutectic (quinary).
Alloy B_3: Mo_{ss} (primary) → Mo_{ss} + T_2 + TiC + Mo_2C eutectic (secondary).
Alloy B_4: T_2 (primary) → Mo_{ss} + T_2 eutectic (secondary) → Mo_{ss} + T_2 + Mo_2C eutectic (tertiary).

The densities of the Mo-Si-B alloys were largely reduced by the addition of TiC. For example, if B_4 did not contain any Ti and C and assuming that Mo_{ss} was pure Mo and T_2 had the stoichiometric composition, the volume fraction of B_4 (Mo_{ss}: 36 pct, T_2: 64 pct in this case) shown in Figure 11(b) would give a density of 9.35 g/cm^3. Furthermore, if the volume fraction of Mo_{ss} was higher than that of B_4, the density value would become higher than 9.35 g/cm^3. Interestingly, the densities of all the alloys examined in this study were lower than 9.01 g/cm^3. In particular, the densities of A_1 and A_2 are 8.80 and 8.70 g/cm^3, respectively, but the Mo_{ss} volume fraction is about 61 pct in A_1 and 56 pct in A_2. Alloy A_3 has a Mo_{ss} volume fraction of about 46 pct and a density of 8.78 g/cm^3. It should be noted that the densities of A_1, A_2, and A_3 are lower than those of the series B alloys, whereas the Mo_{ss} volume fractions are higher than those of the series B alloys except for that of B_2. The low density values would be attained by not only the incorporation of the light phase TiC but also the phase equilibrium of TiC with other phases accompanying a concentration of Ti solutes in Mo_{ss} and T_2.[18,21–23] Therefore, the addition of TiC is effective for enhancing the Mo_{ss} volume fraction and reducing the density of the Mo-Si-B alloys. Kruzic *et al.*[15] pointed out that the fracture toughness of the Mo-Si-B alloys improves with an increase in the Mo_{ss} volume fraction and reaches 12 to 13 MPa(m)$^{1/2}$ at room temperature for a Mo_{ss} volume fraction of around 50 pct. The TiC addition may balance the fracture toughness and density.

The compressive strength of the TiC-added Mo-Si-B alloys appears to be mainly affected by the volume fraction of T_2 + Mo_2C. Although the deformation behavior of the Mo_2C phase is still unclear, it showed good deformability at 1673 K (1400 °C), as seen in Figure 15. However, the plastic deformation of the T_2 phase was poor under the present test conditions: Significant microcracking led to the observed flow stress-lowering behavior. These results strongly suggest that T_2 has a more dominant effect than Mo_2C on the compressive strength of the TiC-added Mo-Si-B alloys. For the series A alloys, the UCS increased monotonically as the composition changed from that of A_1 to A_4, whereas the 0.2 pct proof stress did not vary between the alloys. The variation in the UCS of the series A alloys simply corresponds to the change in the volume fraction of T_2 + Mo_2C. In contrast, the yielding behavior of the alloys is strongly related to the yielding and work-hardening behavior of Mo_{ss}, which are affected by not only the volume fraction but also the size, morphology, and distribution of the Mo_{ss} phase. For the series B alloys, the increase and decrease of the UCS almost corresponded to the behavior of the 0.2 pct proof stress. Furthermore, these variations were quite similar to those of the volume fraction of T_2 + Mo_2C and the inverse volume fraction of Mo_{ss}. Therefore, the variation in the 0.2 pct proof stress and UCS of the series B alloys corresponds to the change in the volume fractions of Mo_{ss} and T_2 + Mo_2C. The volume fraction of TiC in the series B alloys simply decreases as the composition changes from that of B_1 to B_4 and appears not to have a large influence on the compressive strength. However, as mentioned in the discussion concerning Figures 9(c) and (d), TiC appears to prevent interfacial boundary migration and improve the microstructure stability of the alloys. This effect may be advantageous for improving the high-temperature creep strength. Further works will be required to clarify the high-temperature creep strength and its deformation mechanism for the TiC-added Mo-Si-B alloys. The TiC completely decomposed during solidification in the alloy B_4 as seen in Figure 5(d), and it is clear that considerable amounts of decomposed C form Mo_2C, while a large amount of the decomposed Ti probably dissolves into the Mo_{ss} and T_2 phases.[18,21–23] The dissolved Ti should harden both by solid-solution hardening. However, the effect of the dissolved Ti on the high-temperature strength has not yet been revealed. Further studies on the partitioning behavior of Ti and C and the effect of solid-solution hardening by Ti and C on the fracture toughness and high-temperature creep strength are also required for TiC-added Mo-Si-B alloys.

V. CONCLUSIONS

In this study, various amounts of TiC were added into Mo-rich Mo-Si-B alloys, and the phase equilibria,

microstructures, and high-temperature compressive strength of the alloys were investigated. Several kinds of eutectic reactions during solidification were identified, such as $Mo_{ss} + TiC$, $Mo_{ss} + T_2$, $Mo_{ss} + T_2 + TiC$, $Mo_{ss} + T_2 + Mo_2C$, and $Mo_{ss} + T_2 + TiC + Mo_2C$, as well as the crystallization of Mo_{ss}, T_2, or TiC as the primary or tertiary phase. The Mo_{ss}, T_2, TiC, and Mo_2C phases were stably equilibrated even after the heat treatment at 2073 K (1800 °C) for 24 hours. The microstructure evolution and coarsening of the alloys without TiC crystallization developed through the heat treatment, and thus the TiC is considered to prevent interfacial boundary migration and improve the microstructure stability of the alloys. The TiC-added Mo-Si-B alloys have densities of 8.70 to 9.01 g/cm^3, which are within the range of Ni-base superalloys, indicating that TiC addition is very effective for reducing the weight of the Mo-Si-B alloys. The stress–strain curves obtained at 1673 K (1400 °C) and 2×10^{-4} s^{-1} revealed the constant flow stress or UCS followed by flow stress-lowering behavior after yielding and work hardening. The 0.2 pct proof stress and constant flow stress or UCS changed with changes in the composition and are likely to mainly depend on the volume fraction of the Mo_{ss} and T_2 phases. The UCS was shown to increase when the alloys have a high volume fraction of $T_2 + Mo_2C$, and the maximum value exceeded 1 GPa (124 MPa/(g/cm^3)). However, the alloys exhibited a decrease in the flow stress after the UCS due to microcracking within T_2.

ACKNOWLEDGMENTS

This work was supported by the funding program for Next Generation World-Leading Researchers (NEXT Program) (No. GR017) and a Grant-in-Aid for Scientific Research (No. 23-4805) from the Japan Society for the Promotion of Science (JSPS).

REFERENCES

1. D.M. Dimiduk and J.H. Perepezko: *MRS Bull.*, 2003, vol. 28, pp. 639–45.
2. R. Mitra: *Int. Mater. Rev.*, 2006, vol. 51, pp. 13–64.
3. M. Heilmaier, M. Krüger, H. Saage, J. Rösler, D. Mukherji, U. Glatzel, R. Völkl, R. Hüttner, G. Eggeler, Ch. Somsen, T. Depka, H.-J. Christ, B. Gorr, and S. Burk: *J. Met.*, 2009, vol. 61, pp. 61–67.
4. C.A. Nunes, R. Sakidja and J.H. Perepezko: in *Structural Intermetallics*, M.V. Nathal, R. Darolia, C.T. Liu, P.L. Martin, D.B. Miracle, R. Wagner, and M. Yamaguchi, TMS, Warrendale, PA, 1997, pp. 831–39.
5. Y. Yang and Y.A. Chang: *Intermetallics*, 2005, vol. 13, pp. 121–28.
6. J.H. Schneibel, C.T. Liu, D.S. Easton, and C.A. Carmichael: *Mater. Sci. Eng. A*, 1999, vol. 261, pp. 78–83.
7. J.H. Schneibel, M.J. Kramer, and D.S. Easton: *Scripta Mater.*, 2002, vol. 46, pp. 217–21.
8. K. Yoshimi, S. Nakatani, N. Nomura, and S. Hanada: *Intermetallics*, 2003, vol. 11, pp. 787–94.
9. K. Ito, K. Ihara, K. Tanaka, M. Fujikura, and M. Yamaguchi: *Intermetallics*, 2001, vol. 9, pp. 591–602.
10. K. Ito, M. Kumagai, T. Hayashi, and M. Yamaguchi: *Scripta Mater.*, 2003, vol. 49, pp. 285–290.
11. A.P. Alur, N. Chollacoop, and K.S. Kumar: *Acta Mater.*, 2004, vol. 52, pp. 5571–87.
12. P. Jain and K.S. Kumar: *Acta Mater.*, 2010, vol. 58, pp. 2124–42.
13. K. Yoshimi, S. Nakatani, T. Suda, S. Hanada, and H. Habazaki: *Intermetallics*, 2002, vol. 10, pp. 407–14.
14. F.A. Rioult, S.D. Imhoff, R. Sakidja, and J.H. Perepezko: *Acta Mater.*, 2009, vol. 57, pp. 4600–13.
15. J.J. Kruzic, J.H. Schneibel, and R.O. Ritchie: *Metall. Mater. Trans. A*, 2005, vol. 36A, pp. 2393–402.
16. A. Sato, A.-C. Yeh, T. Kobayashi, T. Yokokawa, H. Harada, T. Murakumo, and J.X. Zhang: *Energy Mater.*, 2007, vol. 2, pp. 19–25.
17. R.A. Lula: *Heat-Resistant Materials*, ASM International, Materials Park, OH, 1997, pp. 361–82.
18. V.N. Eremenko and T.Ya. Velikanova: *Handbook of Ternary Alloy Phase Diagrams*, Metals Park, OH, ASM International, 1995, vol. 6, p. 7092.
19. H. Kurishita, Reiji Matsubara, J. SHiraishi, and H. Yoshinaga: *Mater. Trans. JIM*, 1986, vol. 27, pp.858–69.
20. W.M. Haynes: *Handbook of Chemistry and Physics*, 93th ed., CRC Press, Boca Raton, FL, 2012, pp. 4–96.
21. Y. Yang, Y.A. Chang, L. Tan, and W. Cao: *Acta Mater.*, 2005, vol. 53, pp. 1711–20.
22. R. Sakidja and J.H. Perepezko: *Metall. Mater. Trans. A*, 2005, vol. 36A, pp. 507–14.
23. R. Sakidja and J.H. Perepezko: *J. Nucl. Mater.*, 2007, vol. 366, pp. 407–16.